

A stabilized conforming nodal integration for Galerkin mesh-free methods

Jiun-Shyan Chen^{*,†,‡}, Cheng-Tang Wu[§], Sangpil Yoon[¶] and Yang You^{||}

*The Department of Mechanical Engineering and Center for Computer-Aided Design, The University of Iowa,
2137 SC, Iowa City, IA 52242-1527, U.S.A.*

SUMMARY

Domain integration by Gauss quadrature in the Galerkin mesh-free methods adds considerable complexity to solution procedures. Direct nodal integration, on the other hand, leads to a numerical instability due to under integration and vanishing derivatives of shape functions at the nodes. A strain smoothing stabilization for nodal integration is proposed to eliminate spatial instability in nodal integration. For convergence, an integration constraint (IC) is introduced as a necessary condition for a linear exactness in the mesh-free Galerkin approximation. The gradient matrix of strain smoothing is shown to satisfy IC using a divergence theorem. No numerical control parameter is involved in the proposed strain smoothing stabilization. The numerical results show that the accuracy and convergent rates in the mesh-free method with a direct nodal integration are improved considerably by the proposed stabilized conforming nodal integration method. It is also demonstrated that the Gauss integration method fails to meet IC in mesh-free discretization. For this reason the proposed method provides even better accuracy than Gauss integration for Galerkin mesh-free method as presented in several numerical examples. Copyright © 2001 John Wiley & Sons, Ltd.

KEY WORDS: mesh-free; element-free Galerkin; reproducing kernel; nodal integration; stabilization

1. INTRODUCTION

Mesh-free methods can be classified collectively as a Galerkin mesh-free method [1–7], a Petrov–Galerkin mesh-free method [8], or a collocation mesh-free method [9, 10]. Gauss integration is commonly used in Galerkin mesh-free methods for integration of weak form. Due to the complexity involved in Gauss integration for Galerkin mesh-free methods, attempts have been made to develop nodal integration methods for mesh-free computation.

*Correspondence to: Jiun-Shyan Chen, Department of Mechanical Engineering, The University of Iowa, 2137 SC, Iowa City, IA 52242-1527, U.S.A.

†E-mail: jschen@icamen.uiowa.edu

‡Associate Professor

§Postdoctoral Fellow

¶Graduate student

||Graduate student

Contract/grant sponsor: NSF; contract/grant number: CMS 97-13842

Contract/grant sponsor: NSF/DARPA OPAAL Program: DMS 98-74015

Received 13 September 1999

Revised 14 February 2000

Beissel and Belytschko [11] proposed a stabilized nodal integration procedure by adding a residual of the equilibrium equation to the potential energy functional in an element-free Galerkin (EFG) framework. In this study they have shown that the unstabilized EFG with nodal integration displays spurious near-singular modes in some problems. For problems that do not contain unstable modes in their original solution, however, the addition of stabilization actually deteriorates the accuracy. The selection of an effective stabilization parameter also requires some numerical experiments. Another study by Dolbow and Belytschko [12] re-examined the error of Gauss integration in Galerkin mesh-free methods. They demonstrated that considerable integration error is produced when quadrature cells do not match shape function support. A ‘meshing’ strategy was proposed to minimize integration error in Galerkin mesh-free methods.

Randles *et al.* [13] proposed a stress point method to improve performance of smooth particle hydrodynamics (SPH) with collocation. Two sets of points were created for domain discretization, one carries velocity, and another carries stress. Moving least-squares shape functions are constructed at nodes, and velocity at the same set of points are computed. The velocity gradient and stress are computed on stress points using velocity point information, and stress divergence is in turn evaluated at the velocity points using stress point neighbours. The idea is to compute derivatives away from the centroid of the support where kernel functions have zero derivatives. The method improves accuracy and reduces spurious oscillation in SPH with collocation.

Bonet and Kulasegaram [14] introduced an integration correction to improve the accuracy of nodal integration. For linear patch test, correction terms are added to the shape function derivatives. The coefficients of correction terms at discrete nodes are solved by satisfying a linear patch test condition using an iterative procedure. A least-squares stabilization method similar to the method by Beissel and Belytschko [11] was introduced to eliminate spurious modes in nodal integration. To avoid taking a second-order derivative of shape functions in the stabilization terms, a correction procedure is directly applied to the gradient term. This derivative correction is similar to the differential consistency introduced by Belytschko *et al.* [15]

The concept of computing derivatives away from nodes that carry primary variables has also been introduced in a finite difference framework. Breiitkopf *et al.* [16] have recently proposed a so-called double-grid diffuse collocation method. The method is an improvement over the collocation approach originally introduced by Liszka and Orkisz [17] in the generalized finite difference method (GFDM). In Reference [16], the second-order differentiation scheme is replaced by two first-order schemes. The domain is discretized by a set of nodes that carry primary unknown variables, and another set of evaluation points compute the first-order derivatives of the primary unknown variables. The evaluation of equilibrium equation that requires another first-order differentiation is then performed at nodes using the first-order derivatives of primary unknowns computed at the evaluation points. This approach avoids taking derivatives of moving least-squares (MLS) shape functions at nodes.

The objective of this work is to develop a stabilized nodal integration for the Galerkin mesh-free method to achieve higher efficiency with desired accuracy and convergent properties. A strain smoothing stabilization is introduced to compute nodal strain by a divergence counterpart of a spatial averaging of strain. This strain smoothing avoids evaluating derivatives of mesh-free shape functions at nodes and thus eliminates spurious modes. The resulting smoothed gradient matrix is shown to satisfy linear exactness in the Galerkin approximation of a second-order partial differential equation. This strain smoothing approximation is introduced into a Galerkin method via an assumed strain method.

The outline of this paper is as follows. The mesh-free discretization is first reviewed in Section 2. An integration constraint (IC) for numerical integration of weak form in Galerkin approximation is introduced in Section 3. A strain smoothing equation to eliminate spurious modes and to meet IC is introduced in Section 4. The mesh-free discretization using smoothed strain approximation is presented in Section 5. A simple discretization of the smoothed gradient matrix is also discussed. Section 6 demonstrates the effectiveness of the proposed method by analysing several numerical examples. Conclusions and future work are discussed in Section 7.

2. MESH-FREE APPROXIMATION

The two most commonly used approximation theories in mesh-free methods are the moving-least-squares (MLS) approximation in the element-free Galerkin (EFG) method [2], and the reproducing kernel (RK) approximation in the reproducing kernel particle method (RKPM) [3]. Since these two methods lead to an identical approximation when monomial basis functions are used, a reproducing kernel approximation is introduced as a basis to formulate the mesh-free discrete equations in this work.

The discrete RK approximation of a variable u , denoted by u^h , is

$$u^h(\mathbf{x}) = \sum_{I=1}^{NP} \bar{w}_a^{[n]}(\mathbf{x}; \mathbf{x} - \mathbf{x}_I) d_I \tag{1}$$

where NP is the number of points, the superscript n refers to the order of completeness in this approximation, d_I are the coefficients of the approximation, and $\bar{w}_a^{[n]}(\mathbf{x}; \mathbf{x} - \mathbf{x}_I)$ is called the reproducing kernel that is formed by a multiplication of two functions

$$\bar{w}_a^{[n]}(\mathbf{x}; \mathbf{x} - \mathbf{x}_I) = C^{[n]}(\mathbf{x}; \mathbf{x} - \mathbf{x}_I) w_a(\mathbf{x} - \mathbf{x}_I) \tag{2}$$

where $w_a(\mathbf{x} - \mathbf{x}_I)$ is a kernel function that defines the smoothness of the approximation with a compact support measured by ‘ a ’, and $C^{[n]}(\mathbf{x}; \mathbf{x} - \mathbf{x}_I)$ is an enrichment function (also called a correction function) that is used to satisfy the n th-order reproducing conditions

$$\sum_{I=1}^{NP} \bar{w}_a^{[n]}(\mathbf{x}; \mathbf{x} - \mathbf{x}_I) x_{1I}^p x_{2I}^q = x_1^p x_2^q \quad \text{for } p + q = 0, \dots, n \quad (x_1 \equiv x, \quad x_2 \equiv y) \tag{3}$$

where x_{iI} is the value of x_i at node I .

To meet the n th-order reproducing conditions of Equation (3), the enrichment function $C^{[n]}(\mathbf{x}; \mathbf{x} - \mathbf{x}_I)$ is constructed by a linear combination of complete n th-order monomial functions

$$\begin{aligned} C^{[n]}(\mathbf{x}; \mathbf{x} - \mathbf{x}_I) &= \sum_{p+q=0}^n (x_1 - x_{1I})^p (x_2 - x_{2I})^q b_{pq}(\mathbf{x}) \\ &\equiv \mathbf{H}^{[n]\top}(\mathbf{x} - \mathbf{x}_I) \mathbf{b}(\mathbf{x}) \end{aligned} \tag{4}$$

where $b_{pq}(\mathbf{x})$ are the coefficients of the monomial basis functions that are functions of \mathbf{x} , $\mathbf{b}(\mathbf{x})$ is a vector of $b_{pq}(\mathbf{x})$, and $\mathbf{H}^{[n]}(\mathbf{x} - \mathbf{x}_I)$ is a vector containing the monomial basis functions

$$\mathbf{H}^{[n]\top}(\mathbf{x} - \mathbf{x}_I) = [1, x_1 - x_{1I}, x_2 - x_{2I}, (x_1 - x_{1I})^2, \dots, (x_2 - x_{2I})^n] \tag{5}$$

Substituting Equation (4) into Equation (3), the coefficients $\mathbf{b}(\mathbf{x})$ are solved by

$$\mathbf{M}^{[n]}(\mathbf{x})\mathbf{b}(\mathbf{x}) = \mathbf{H}(\mathbf{0}) \quad (6)$$

where

$$\mathbf{M}^{[n]}(\mathbf{x}) = \sum_{I=1}^{\text{NP}} \mathbf{H}^{[n]}(\mathbf{x} - \mathbf{x}_I) \mathbf{H}^{[n]\top}(\mathbf{x} - \mathbf{x}_I) w_a(\mathbf{x} - \mathbf{x}_I) \quad (7)$$

$\mathbf{M}^{[n]}(\mathbf{x})$ is the moment matrix of $w_a(\mathbf{x} - \mathbf{x}_I)$. For $\mathbf{M}^{[n]}(\mathbf{x})$ in Equation (6) to be invertible, the support of $w_a(\mathbf{x} - \mathbf{x}_I)$ needs to be greater than a minimum size that is related to the order of basis functions used in the enrichment function $C^{[n]}(\mathbf{x}; \mathbf{x} - \mathbf{x}_I)$ and the nodal spacing, and $w_a(\mathbf{x} - \mathbf{x}_I)$ must be a positive function within the support. Using the solution of Equations (2), (4) and (6), the reproducing kernel approximation is obtained by

$$u^h = \sum_{I=1}^{\text{NP}} \mathbf{H}^{[n]\top}(\mathbf{0}) \mathbf{M}^{[n]-1}(\mathbf{x}) \mathbf{H}^{[n]}(\mathbf{x} - \mathbf{x}_I) w_a(\mathbf{x} - \mathbf{x}_I) d_I \equiv \sum_{I=1}^{\text{NP}} \Psi_I(\mathbf{x}) d_I \quad (8)$$

where $\Psi_I(\mathbf{x})$ are the RK shape functions of the approximation

$$\Psi_I(\mathbf{x}) = \mathbf{H}^{[n]\top}(\mathbf{0}) \mathbf{M}^{[n]-1}(\mathbf{x}) \mathbf{H}^{[n]}(\mathbf{x} - \mathbf{x}_I) w_a(\mathbf{x} - \mathbf{x}_I) \quad (9)$$

and $\Psi_I(\mathbf{x})$ are n th-order complete, i.e.

$$\sum_{I=1}^{\text{NP}} \Psi_I(\mathbf{x}) x_1^p x_2^q = x_1^p x_2^q \quad \text{for } p + q = 0, \dots, n \quad (10)$$

$$\sum_{I=1}^{\text{NP}} D_{ij}(\Psi_I(\mathbf{x})) x_1^p x_2^q = D_{ij}(x_1^p x_2^q) \quad \text{for } p + q = 0, \dots, n \quad (11)$$

where $D_{ij}(\cdot) \equiv \partial^{i+j}(\cdot) / \partial x_1^i \partial x_2^j$ is a differential operator.

When monomial basis functions are used in the reproducing kernel approximation, the smoothness and compact support properties of the shape function $\Psi_I(\mathbf{x})$ are identical to those of the kernel function $w_a(\mathbf{x} - \mathbf{x}_I)$. Commonly used kernel functions are exponential functions, Gaussian function, and B-spline functions. The multi-dimensional kernel functions can be constructed by using the product of one-dimensional shape functions, or by considering the distance between nodes $|\mathbf{x} - \mathbf{x}_I|$ as an independent variable in the evaluation of the kernel functions (see References [1–3] for details).

Note that, in general, the shape functions $\Psi_I(\mathbf{x})$ do not bear Kronecker delta properties, and therefore discretization of a PDE using Galerkin approximation with mesh-free shape functions requires special treatment. Methods such as coupling with finite elements [18], transformation methods [4, 9], and the boundary singular kernel method [19] have been proposed. These methods allow for a direct imposition of essential boundary conditions, and the approximation of displacement can be made kinematically admissible.

3. INTEGRATION CONSTRAINT

The convergence of the Galerkin method for a partial differential equation is determined by approximation for the unknowns and the numerical integration of the weak form. Shape functions with linear consistency can be obtained from moving least-squares (MLS) approximation or reproducing kernel (RK) approximation with linear basis functions. The employment of linearly consistent shape functions in the Galerkin approximation, however, does not guarantee a linear exactness in the solution of the Galerkin method. Additional requirements associated with the domain integration of the Galerkin mesh-free method are discussed in this section.

For demonstration purposes, consider the following static equilibrium equation in elasticity with zero body force:

$$\sigma_{ij,j} = 0 \quad \text{in } \Omega \tag{12a}$$

$$\sigma_{ij} = C_{ijkl}\varepsilon_{kl}, \quad \varepsilon_{ij} = \frac{1}{2}(u_{i,j} + u_{j,i}) \equiv \nabla^S(u)_{ij} \tag{12b}$$

with boundary conditions

$$u_i = g_i \quad \text{on } \Gamma^g \tag{12c}$$

$$\sigma_{ij}n_j = h_i \quad \text{on } \Gamma^h \tag{12d}$$

where Ω is the problem domain with essential boundary Γ^g and natural boundary Γ^h , u_i is the displacement, C_{ijkl} is the elasticity tensor, n_i is the surface normal, and h_i is the surface traction. The variational equation of (12a) is

$$\int_{\Omega} \delta \nabla^S(u)_{ij} C_{ijkl} \nabla^S(u)_{kl} \, d\Omega - \int_{\Gamma^h} \delta u_i h_i \, d\Gamma = 0 \tag{13}$$

In a static equilibrium (12a), if essential boundary conditions are prescribed as a linear function $g_i(x, y) = a_{i0} + a_{i1}x + a_{i2}y$, and natural boundary conditions are assigned as $h_i = \sigma_{ij}n_j$ with stress σ_{ij} computed from $u_i(x, y) = a_{i0} + a_{i1}x + a_{i2}y$, then the solution of (12) is the same linear function: $u_i(x, y) = a_{i0} + a_{i1}x + a_{i2}y$.

For linear exactness in Galerkin approximation, the approximation of displacement $u_i^h = \sum_{l=1}^{NP} \Psi_l d_{il}$ in the variational equation with the above-mentioned boundary conditions must generate a linear discrete solution. This is equivalent to requiring that a linear discrete solution $u_i^h = \sum_{l=1}^{NP} \Psi_l d_{il}$ with $d_{il} = a_{i0} + a_{i1}x_l + a_{i2}y_l$ exactly satisfies the discrete equilibrium associated with Equation (13) when essential and natural boundary conditions are prescribed based on a linear displacement field $u_i(x, y) = a_{i0} + a_{i1}x + a_{i2}y$. This first requires that the shape functions satisfy linear consistency of Equation (10). Next, let \mathbf{d} be the vector of a linear function $a_{i0} + a_{i1}x + a_{i2}y$, i.e. let the I th component of \mathbf{d} be

$$\mathbf{d}_I = \begin{bmatrix} a_{i0} + a_{i1}x_I + a_{i2}y_I \\ a_{20} + a_{21}x_I + a_{22}y_I \end{bmatrix} \tag{14}$$

then the internal force computed using a linear displacement vector in Equation (14) is

$$\mathbf{f}_I^{\text{int}} = \int_{\Omega} \mathbf{B}_I^T \mathbf{C} \mathbf{B} \mathbf{d} \, d\Omega = \int_{\Omega} \mathbf{B}_I^T \mathbf{C} \mathbf{B} \mathbf{d} \, d\Omega = \int_{\Omega} \mathbf{B}_I^T \mathbf{C} \boldsymbol{\varepsilon}^C \, d\Omega \quad (15)$$

where \mathbf{B}_I is the standard gradient matrix, and $\boldsymbol{\varepsilon}^C$ is a constant strain vector (the components of $\boldsymbol{\varepsilon}^C$ are not functions of x and y). To arrive at a constant strain we have used linear consistency and its derivatives in Equations (10)–(11) for $n=1$. Equation (15) can further be manipulated as

$$\mathbf{f}_I^{\text{int}} = \int_{\Omega} \mathbf{B}_I^T \boldsymbol{\sigma}^C \, d\Omega = \int_{\Omega} \mathbf{B}_I^T \, d\Omega \boldsymbol{\sigma}^C \quad (16)$$

where $\boldsymbol{\sigma}^C$ is a constant stress vector and can be moved outside the integration. Note that a_{ij} in Equation (14) are arbitrary, and therefore $\boldsymbol{\sigma}^C$ is an arbitrary constant vector. If a natural boundary condition is given by $h_i = \sigma_{ij}^C n_j$ with $\boldsymbol{\sigma}^C$ the constant stress computed using the same linear displacement vector $u_i(x, y) = a_{i0} + a_{i1}x + a_{i2}y$, the external force of Galerkin approximation is

$$\mathbf{f}_I^{\text{ext}} = \int_{\Gamma^h} \mathbf{N}_I^T \boldsymbol{\sigma}^C \, d\Gamma = \int_{\Gamma^h} \mathbf{N}_I^T \, d\Gamma \boldsymbol{\sigma}^C \quad (17)$$

$$\mathbf{N}_I = \begin{bmatrix} \Psi_I n_1 & 0 \\ 0 & \Psi_I n_2 \\ \Psi_I n_2 & \Psi_I n_1 \end{bmatrix} \quad (18)$$

Satisfying discrete equilibrium using Equations (16) and (17) requires

$$\int_{\Omega} \mathbf{B}_I^T \, d\Omega \boldsymbol{\sigma}^C = \int_{\Gamma^h} \mathbf{N}_I^T \, d\Gamma \boldsymbol{\sigma}^C \quad (19)$$

Since $\boldsymbol{\sigma}^C$ is arbitrary, for interior nodes Equation (19) reduces to

$$\int_{\Omega} \mathbf{B}_I^T \, d\Omega = \mathbf{0} \quad \text{for all interior nodes } \{I: \text{supp}(\Psi_I) \cap \Gamma = \emptyset\} \quad (20)$$

If numerical integration is employed in the variational Equation (13), the resulting discrete equation of Equation (20) is

$$\sum_{L=1}^{\text{NIT}} \mathbf{B}_I(\mathbf{x}_L) \omega_L = \mathbf{0} \quad \text{for all interior nodes } \{I: \text{supp}(\Psi_I) \cap \Gamma = \emptyset\} \quad (21)$$

where NIT is the number of integration points. In the Gauss quadrature rule, \mathbf{x}_L are the spatial co-ordinates of Gauss points that are determined using a three-sided or four-sided background grid, and ω_L are the weights of Gauss quadrature. If nodal integration methods are employed, \mathbf{x}_L is the spatial location of discrete nodes, and ω_L are the associated weights at nodes that vary with the type of integration methods employed.

For shape functions that intersect with natural boundary for arbitrary $\boldsymbol{\sigma}^C$, the numerical integration counterpart of Equation (19) is

$$\sum_{L=1}^{\text{NIT}} \mathbf{B}_I(\mathbf{x}_L) \omega_L = \sum_{L=1}^{\text{NITh}} \mathbf{N}_I(\mathbf{x}_L) s_L \quad \text{for boundary nodes } \{I: \text{supp}(\Psi_I) \cap \Gamma^h \neq \emptyset\} \quad (22)$$

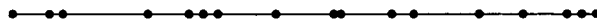


Figure 1. Irregular discretization of a one-dimensional domain.

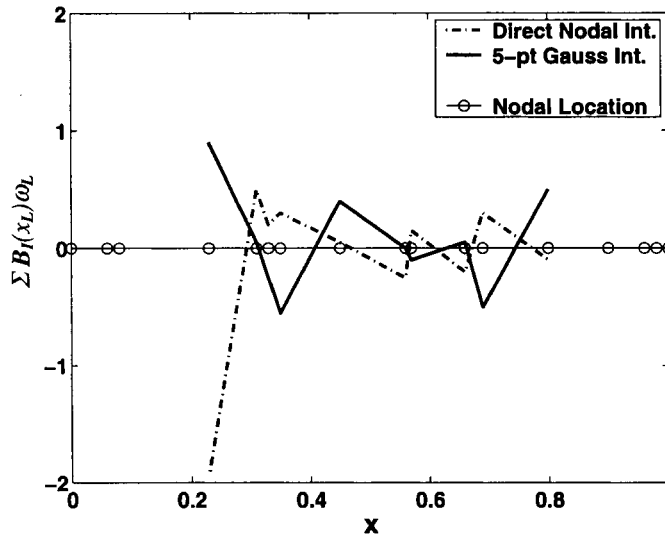


Figure 2. Violation of IC in direct nodal integration and five-point Gauss integration.

where s_L are the weights of boundary integration, and NITH is the number of integration points on the natural boundary. We call Equations (21) and (22) the integration constraints (IC). If the whole problem boundary is essential boundary, then only Equation (21) needs to be satisfied. Similar results have been obtained by Krongauz and Belytschko [20] and Bonet and Kulasegaram [14]. A normalization of discrete gradient in SPH has also been discussed by Johnson and Beissel [21] and Randles and Libersky [10].

The following problem is presented to demonstrate how the violation in IC is related to error in a linear solution:

$$u_{,xx} = 0, \quad 0 \leq x \leq 1 \tag{23a}$$

$$u(0) = 0, \quad u(1) = 1 \tag{23b}$$

The domain $0 \leq x \leq 1$ is discretized by 17 irregular points as shown in Figure 1. The open circles in the figure represent nodal locations. The RK shape functions with linear polynomial basis are used in the Galerkin approximation. Two integration methods are examined: (1) a five-point Gauss integration and, (2) a direct nodal integration using trapezoidal rule. Since the maximum nodal distance in the model is 0.145, shape functions with constant support size of 0.15 are used.

The violation of integration constraint (IC) in Equation (21) using both integration methods is shown in Figure 2. Both trapezoidal rule and five-point Gauss integration violate IC. The consequence of violating IC is the cause of error in the linear solution $u = x$ of this problem as shown in Figures 3 and 4. The trapezoidal rule displays a significant error in u and du/dx . Gauss integration improves accuracy in u considerably, but still presents noticeable error in du/dx (Figure 4).

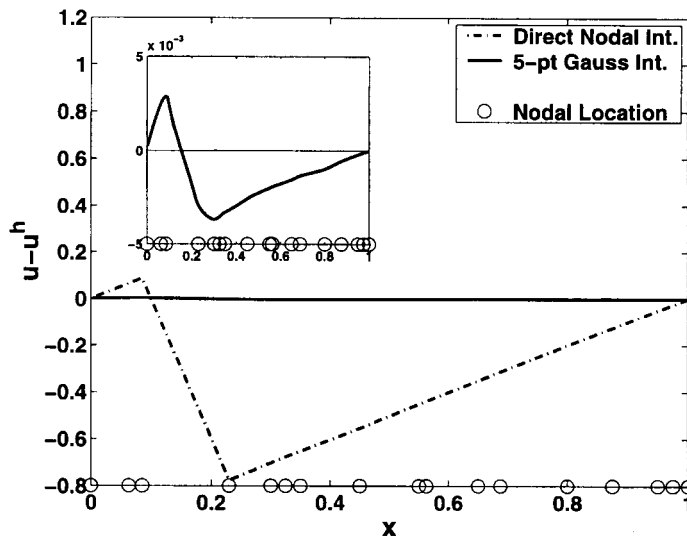


Figure 3. Errors in linear u using direct nodal integration and five-point Gauss integration.

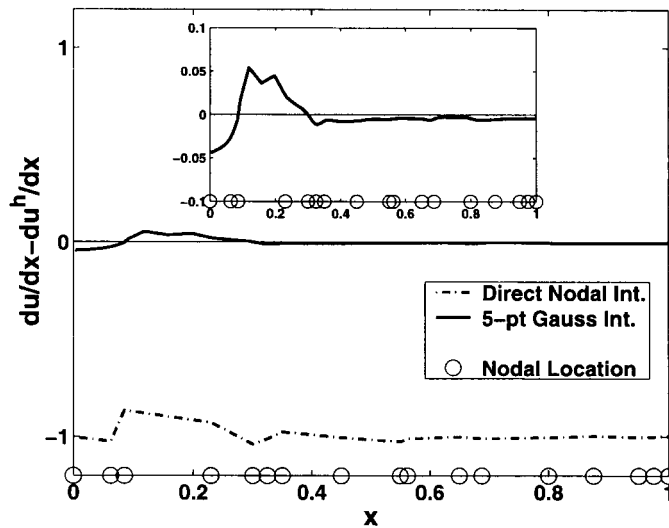


Figure 4. Errors in constant du/dx using direct nodal integration and five-point Gauss integration.

4. STRAIN SMOOTHING STABILIZATION

A strain smoothing method was proposed by Chen *et al.* [22, 23] as a regularization for material instabilities in strain localization. For stabilization in nodal integration, a modified strain smoothing at a node is proposed in this paper by

$$\tilde{\varepsilon}_{ij}^h(\mathbf{x}_L) = \int_{\Omega} \tilde{\varepsilon}_{ij}^h(\mathbf{x}) \Phi(\mathbf{x}; \mathbf{x} - \mathbf{x}_L) d\Omega \quad (24)$$

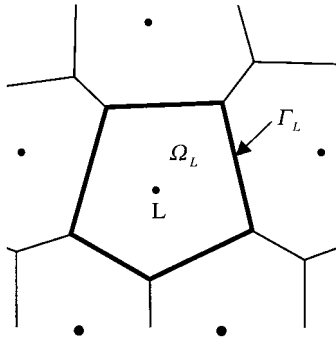


Figure 5. Example of Voronoi diagram in two dimensions.

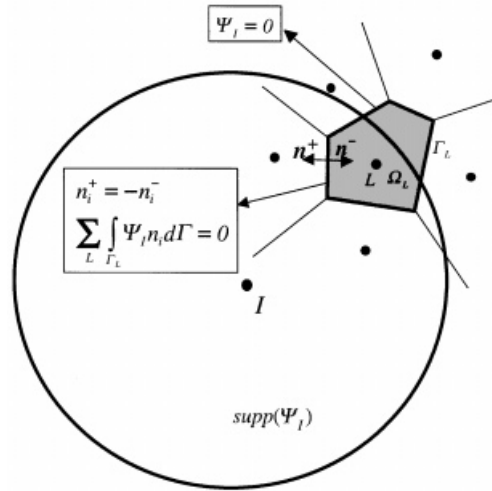


Figure 6. Geometric relationship between $\text{supp}(\Psi_I)$ and representative nodal domain Ω_L .

where ε_{ij} is the strain obtained from displacement by compatibility, $\varepsilon_{ij}^h = (u_{i,j}^h + u_{j,i}^h)/2$, and Φ is a distribution function. Consider a *weighted* Shepard function as a distribution function

$$\Phi(\mathbf{x}; \mathbf{x} - \mathbf{x}_L) = \frac{\phi(\mathbf{x} - \mathbf{x}_L)}{\sum_{J=1}^{NP} \phi(\mathbf{x} - \mathbf{x}_J) A_J} \tag{25}$$

where $A_L = \int_{\Omega_L} d\Omega$ is the area (or volume) of the representative domain of node L obtained from, for example, the Voronoi diagram in Figure 5. The weighted Shepard function in Equation (25) satisfies the following *weighted* partition of unity:

$$\sum_{L=1}^{NP} \Phi(\mathbf{x}; \mathbf{x} - \mathbf{x}_L) A_L = 1 \tag{26}$$

For simplicity, a piecewise constant function of ϕ is introduced

$$\phi(\mathbf{x} - \mathbf{x}_L) = \begin{cases} 1, & \mathbf{x} \in \Omega_L \\ 0, & \mathbf{x} \notin \Omega_L \end{cases} \tag{27}$$

and consequently, the distribution function is

$$\Phi(\mathbf{x}; \mathbf{x} - \mathbf{x}_L) = \begin{cases} 1/A_L, & \mathbf{x} \in \Omega_L \\ 0, & \mathbf{x} \notin \Omega_L \end{cases} \tag{28}$$

Substituting Equation (28) into strain smoothing Equation (24), and applying a divergence theorem, the following equation is obtained:

$$\varepsilon_{ij}^h(\mathbf{x}_L) = \int_{\Omega} \frac{1}{2} \left(\frac{\partial u_i^h}{\partial x_j} + \frac{\partial u_j^h}{\partial x_i} \right) \Phi(\mathbf{x}; \mathbf{x} - \mathbf{x}_L) d\Omega$$

$$\begin{aligned}
 &= \frac{1}{2A_L} \int_{\Omega_L} \left(\frac{\partial u_i^h}{\partial x_j} + \frac{\partial u_j^h}{\partial x_i} \right) d\Omega \\
 &= \frac{1}{2A_L} \int_{\Gamma_L} (u_i^h n_j + u_j^h n_i) d\Gamma
 \end{aligned} \tag{29}$$

where Γ_L is the boundary of the representative domain of node L . Introducing RK shape functions into Equation (29) yields

$$\tilde{\boldsymbol{\varepsilon}}^h(\mathbf{x}_L) = \sum_{I \in G_L} \tilde{\mathbf{B}}_I(\mathbf{x}_L) \mathbf{d}_I \tag{30}$$

where G_L is a group of nodes in which their associated shape function supports cover node L . Two dimensions

$$\tilde{\boldsymbol{\varepsilon}}^{h^T} = [\tilde{\varepsilon}_{11}^h, \tilde{\varepsilon}_{22}^h, 2\tilde{\varepsilon}_{12}^h] \quad \mathbf{d}_I^T = [d_{1I}, d_{2I}] \tag{31}$$

$$\tilde{\mathbf{B}}_I(\mathbf{x}_L) = \begin{bmatrix} \tilde{b}_{I1}(\mathbf{x}_L) & 0 \\ 0 & \tilde{b}_{I2}(\mathbf{x}_L) \\ \tilde{b}_{I2}(\mathbf{x}_L) & \tilde{b}_{I1}(\mathbf{x}_L) \end{bmatrix} \tag{32}$$

$$\tilde{b}_{Ii}(\mathbf{x}_L) = \frac{1}{A_L} \int_{\Gamma_L} \Psi_I(\mathbf{x}) n_i(\mathbf{x}) d\Gamma \tag{33}$$

To ensure accuracy and convergence in employing this smoothed strain as a stabilization into Galerkin mesh-free discretization with nodal integration, integration constraints (IC) need to be satisfied. The following discussion examines whether the proposed strain smoothing stabilization satisfies IC. To meet IC using stabilized nodal integration with the smoothed gradient matrix $\tilde{\mathbf{B}}_I$, the following equation must vanish for all interior nodes $\{I: \text{supp}(\psi_I) \cap \Gamma = \emptyset\}$:

$$\sum_L \tilde{\mathbf{B}}_I(\mathbf{x}_L) A_L = \begin{bmatrix} \sum_L \tilde{b}_{I1}(\mathbf{x}_L) A_L & 0 \\ 0 & \sum_L \tilde{b}_{I2}(\mathbf{x}_L) A_L \\ \sum_L \tilde{b}_{I2}(\mathbf{x}_L) A_L & \sum_L \tilde{b}_{I1}(\mathbf{x}_L) A_L \end{bmatrix} = \mathbf{0} \tag{34}$$

and consequently, each component in the matrix of Equation (34) must vanish, i.e.

$$\sum_L \tilde{b}_{Ii}(\mathbf{x}_L) A_L = 0 \tag{35}$$

where

$$\sum_L \tilde{b}_{Ii}(\mathbf{x}_L) A_L = \sum_L \int_{\Gamma_L} \Psi_I(\mathbf{x}) n_i(\mathbf{x}) d\Gamma \tag{36}$$

For Γ_L that is completely or partially inside $\text{supp}(\Psi_I)$, each segment of Γ_L inside $\text{supp}(\Psi_I)$ is shared by two nodal domains with opposite surface normals on each side of the domain as shown in Figure 6. The condition $\mathbf{n}^+(\mathbf{x}) = -\mathbf{n}^-(\mathbf{x})$ for $\mathbf{x} \in \Gamma_L, \mathbf{x} \in \text{supp}(\Psi_I)$ leads to a vanishing summation $\sum_L \int_{\Gamma_L} \Psi_I(\mathbf{x}) n_i(\mathbf{x}) d\Gamma$ in Equation (36). For Γ_L that is completely or partially outside $\text{supp}(\Psi_I)$, $\Psi_I(\mathbf{x}) = 0$ for $\mathbf{x} \in \Gamma_L, \mathbf{x} \notin \text{supp}(\Psi_I)$, and as such the vanishing condition

$\sum_L \int_{\Gamma_L} \Psi_I(\mathbf{x}) n_i(\mathbf{x}) d\Gamma = 0$ remains. Therefore for interior nodes, $\tilde{\mathbf{B}}_I$ exactly satisfy integration constraint of Equation (21), i.e.,

$$\sum_L \tilde{\mathbf{B}}_I(\mathbf{x}_L) A_L = \mathbf{0} \tag{37}$$

In the case where $\text{supp}(\Psi_I)$ intersects with the natural boundary, Equation (36) reduces to

$$\sum_L \tilde{b}_{li}(\mathbf{x}_L) A_L = \sum_L \int_{\Gamma_L \cap \Gamma^h} \Psi_I(\mathbf{x}) n_i(\mathbf{x}) d\Gamma = \int_{\Gamma^h} \Psi_I(\mathbf{x}) n_i(\mathbf{x}) d\Gamma \tag{38}$$

To result in Equation (38), two conditions have been used: (1) $\sum_L \int_{\Gamma_L - \Gamma^h} \Psi_I(\mathbf{x}) n_i(\mathbf{x}) d\Gamma = 0$, and (2) $\Psi_I(\mathbf{x}) = 0$ for $\mathbf{x} \in \Gamma^h$, $\mathbf{x} \notin \text{supp}(\Psi_I)$. In fact, Equation (38) applies to all nodes that intersect with the boundary. The numerical integration on the boundary in Equation (38) leads to the satisfaction of IC in Equation (22).

5. GALERKIN APPROXIMATION AND DISCRETIZATION

To introduce the strain smoothing formulation into the Galerkin approximation, we consider the mixed variational principle based on an assumed strain method [24]:

$$\delta U(\mathbf{u}, \tilde{\boldsymbol{\varepsilon}}) = \int_{\Omega} \delta \tilde{\varepsilon}_{ij} C_{ijkl} \tilde{\varepsilon}_{kl} d\Omega - \int_{\Omega} \delta u_i b_i d\Omega - \int_{\Gamma^h} \delta u_i h_i d\Gamma = 0 \tag{39}$$

where u_i is the displacement vector with $u_i = g_i$ on the essential boundary Γ^g , $\tilde{\varepsilon}_{ij}$ is the assumed strain, b_i is the body force, h_i is the surface traction, and Γ^h is the natural boundary. Displacements and strains are approximated by

$$\mathbf{u}^h = \sum_{I=1}^{NP} \Psi_I \mathbf{d}_I \equiv \Psi \mathbf{d} \tag{40}$$

$$\tilde{\boldsymbol{\varepsilon}}^h = \sum_{I=1}^{NP} \tilde{\mathbf{B}}_I \mathbf{d}_I \equiv \tilde{\mathbf{B}} \mathbf{d} \tag{41}$$

Remark. The moving least-squares (MLS) or reproducing kernel (RK) shape functions Ψ_I do not possess Kronecker delta properties, and for \mathbf{u}^h to be kinematically admissible, a mixed transformation method that transforms the generalized co-ordinate \mathbf{d} to a mixed co-ordinate \mathbf{d}^* for a direct imposition of essential boundary conditions [19] is used

$$\mathbf{d} = \begin{bmatrix} \mathbf{d}^B \\ \mathbf{d}^I \end{bmatrix} = \begin{bmatrix} \Lambda^{BB^{-1}} & \Lambda^{BB^{-1}} \Lambda^{BI} \\ 0 & \mathbf{I} \end{bmatrix} \begin{bmatrix} \hat{\mathbf{d}}^B \\ \mathbf{d}^I \end{bmatrix} \equiv \Lambda^* \mathbf{d}^* \tag{42}$$

where \mathbf{d}^B and \mathbf{d}^I are generalized displacement vectors for boundary and interior degrees of freedom, respectively, $\hat{\mathbf{d}}^B$ is the nodal boundary displacement vector, and Λ^{BB} and Λ^{BI} are transformation matrices associated with boundary degrees of freedom [19]. With this co-ordinate transformation on Equation (40), essential boundary conditions can be directly imposed, and as such the discrete solution space is kinematically admissible.

The assumed strain $\tilde{\boldsymbol{\varepsilon}}^h$ in Equation (41) is approximated by the smoothed gradient matrix $\tilde{\mathbf{B}}$ of Equation (32) and the displacement coefficients \mathbf{d} . A nodal integration of the weak form,

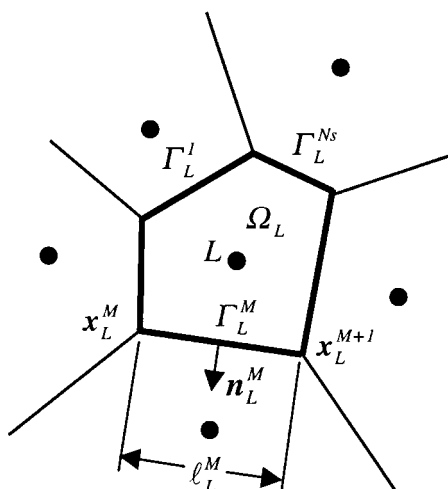


Figure 7. Geometry definition of a representative nodal domain.

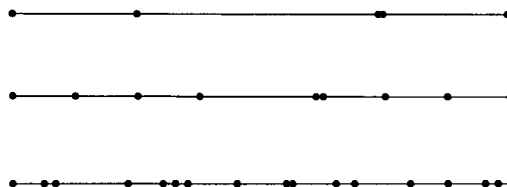


Figure 8. Irregular mesh-free discretization.

Equation (39), requires calculation of $\tilde{\mathbf{B}}$ at nodal location \mathbf{x}_L described in Equations (32) and (33). For nodal evaluation of components $\tilde{b}_{Ii}(\mathbf{x}_L)$ in $\tilde{\mathbf{B}}_I(\mathbf{x}_L)$ using Equation (33), a boundary integration of representative nodal domain is needed. Letting

$$\Gamma_L = \bigcup_{M=1}^{Ns} \Gamma_L^M \tag{43}$$

where Γ_L^M are the boundary segments of Γ_L as shown in Figure 7, and N_s is the total number of segments. Since Equation (37) satisfies integration constraint regardless of the numerical integration employed for $\tilde{b}_{Ii}(\mathbf{x}_L)$, a two-point trapezoidal rule for each segment of the representative nodal boundary Γ_L^M can be considered:

$$\begin{aligned} \tilde{b}_{Ii}(\mathbf{x}_L) &= \int_{\bigcup_{M=1}^{Ns} \Gamma_L^M} \Psi_I(\mathbf{x}) n_i(\mathbf{x}) d\Gamma \\ &= \sum_{M=1}^{Ns} \left[\Psi_I(\mathbf{x}_L^M) n_{iL}^M \frac{\ell_L^M}{2} + \Psi_I(\mathbf{x}_L^{M+1}) n_{iL}^M \frac{\ell_L^M}{2} \right] \end{aligned} \tag{44}$$

As shown in Figure 7, \mathbf{x}_L^M and \mathbf{x}_L^{M+1} are the two end points of boundary segment Γ_L^M , ℓ_L^M is the length of Γ_L^M , i.e. $\ell_L^M = \int_{\Gamma_L^M} d\Gamma$, and \mathbf{n}_L^M is the outward surface normal of Γ_L^M . Note that the node numbers M are defined recursively, i.e. $M = N_s + 1 \rightarrow M = 1$. Since Equation (44) involves only an evaluation of $\Psi_I n_i$ at the vertices of the representative nodal domain, Equation (44) can be re-written as

$$\tilde{b}_{Ii}(\mathbf{x}_L) = \sum_{M=1}^{Ns} \left[\frac{1}{2} (n_{iL}^M \ell_L^M + n_{iL}^{M+1} \ell_L^{M+1}) \Psi_I(\mathbf{x}_L^{M+1}) \right] \tag{45}$$

Again, recursive relation holds: $M = N_s + 1 \rightarrow M = 1$. Note that in Equation (45) no derivatives of the shape functions are involved in evaluating the smoothed gradient matrix at the nodal

points. Trapezoidal rule with more than two points on each segment for integration on Γ_L in Equation (44) can also be employed for better accuracy.

By introducing approximations \mathbf{u}^h and $\tilde{\boldsymbol{\xi}}^h$ and performing nodal integration in the variational equation (39), the following discrete equation is obtained:

$$\mathbf{Kd} = \mathbf{f} \tag{46}$$

$$\mathbf{K}_{IJ} = \sum_{L=1}^{NP} \tilde{\mathbf{B}}_I^T(\mathbf{x}_L) \mathbf{C} \tilde{\mathbf{B}}_J(\mathbf{x}_L) \mathbf{A}_L \tag{47}$$

$$\mathbf{f}_I = \sum_{L=1}^{NP} \Psi_I(\mathbf{x}_L) \mathbf{b}(\mathbf{x}_L) \mathbf{A}_L + \sum_{L=1}^{NPb} \Psi_I(\mathbf{x}_L) \mathbf{h}(\mathbf{x}_L) s_L \tag{48}$$

where NPb is the number of points on the natural boundary, and s_L are the weights associated with the boundary point that can also be obtained from the Voronoi diagram. Note that the summation in Equations (47) and (48) are performed only on the nodes that are covered under the supports of shape functions at nodes I and J .

For imposing the essential boundary conditions using a mixed transformation method, \mathbf{K} and \mathbf{f} are transformed to a mixed co-ordinate

$$\mathcal{H}^* \mathbf{d} = \mathcal{f}^* \tag{49}$$

where

$$\mathcal{H}^* = \mathcal{L}(\mathbf{K}^*) \tag{50}$$

$$\mathcal{f}^* = \ell(\mathbf{f}^*) \tag{51}$$

$$\mathbf{K}^* = \mathbf{\Lambda}^{*-1} \mathbf{K} \tag{52}$$

$$\mathbf{f}^* = \mathbf{\Lambda}^{*-1} \mathbf{f} \tag{53}$$

where \mathcal{L} is a matrix operator that replaces the rows associated with the prescribed boundary degrees of freedom by kinematic constraint equations, ℓ is the vector operator that replaces components associated with boundary constrained degrees of freedom by prescribed displacement values, and $\mathbf{\Lambda}^*$ is the transformation matrix given in Equation (42). For a detailed discussion on the transformation from Equations (46)–(49), refer to Reference [19].

6. NUMERICAL EXAMPLES

In the following examples, unless otherwise specified, mesh-free displacement shape functions are formulated using reproducing kernel approximation with linear consistency. Three integration methods are used for comparison: (1) Gauss integration with 5×5 (or five points in one dimension) quadrature, (2) Direct nodal integration, and (3) the proposed stabilized conforming (SC) nodal integration. The error norms are computed using a 5×5 (or five points in one dimension) Gauss quadrature rule.

6.1. One-dimensional linear problem

The following second-order differential equation is considered:

$$u_{,xx} = 0, \quad 0 \leq x \leq 1 \quad (54)$$

with boundary conditions

$$u(0) = 0, \quad u(1) = 1 \quad (55)$$

Three irregular models shown in Figure 8 are generated for analysis using a five-point Gauss integration, a direct nodal integration, and the proposed stabilized conforming (SC) nodal integration. Shape function support sizes of 0.6, 0.3 and 0.15 are used for the 5-, 9-, and 17-node irregular discrete models in this study. Linear basis functions are used to construct the shape functions. In the first model, the center point is moved to the right side and almost coincides with the adjacent node. The error of numerical solution $u - u^h$ and their derivatives $du/dx - du^h/dx$ using three methods are shown in Figures 9(a) and 9(b). The open circles in the figures represent the nodal locations. Direct nodal integration generates significant error in the linear solution. The Gauss integration method also shows small errors of 10^{-3} in u and du/dx as shown in the zoom-in plots. This indicates that the mesh-free method using Gauss integration does not exactly meet integration constraint (IC). The proposed SC nodal integration method, on the other hand, exactly satisfies IC and obtains an exact solution in this problem.

In the refined 9-node irregular model with the centre point moved to the right side, the errors in the direct nodal integration and the Gauss integration methods are reduced as shown in Figures 10(a) and 10(b). Again, direct nodal integration generates much larger errors compared to those in the other two methods. The use of Gauss integration still shows errors of 10^{-4} and 10^{-3} in u and du/dx , respectively, in the zoom-in plots. The SC nodal integration continues to obtain an exact solution with this irregular model. For the case with a complete irregular discretization, even the Gauss integration method produces significant errors as displayed in Figures 11(a) and 11(b). Conversely, the proposed SC nodal integration still generates excellent solution in u and du/dx .

6.2. Bar subjected to body force

This problem has been studied by Beissel and Belytschko [11] to demonstrate spurious oscillation in the direct nodal integration method. The model problem is

$$u_{,xx} = -100x, \quad 0 \leq x \leq 1 \quad (56)$$

with boundary conditions

$$u(0) = u(1) = 0 \quad (57)$$

Analysis is first performed using shape functions with linear basis. Similar to the observation reported in Reference [11], when linear basis functions are used in displacement shape functions with regular nodal spacing, oscillation in the direct nodal integration does not appear. However, L_2 norms of errors in u and du/dx shown in Figures 12(a) and 12(b), respectively, present considerable errors in the direct nodal integration method; particularly in du/dx . Equally spaced discretization of 11-, 21-, 41-, and 81-node with a normalized support size of 1.5 is used in this convergence

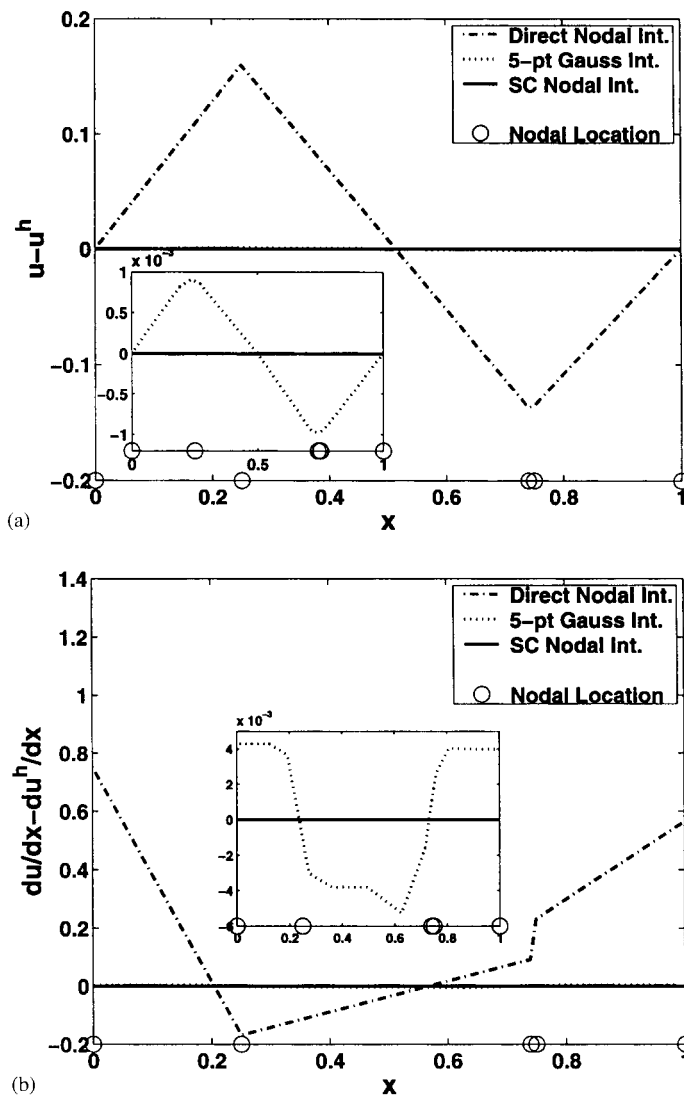


Figure 9. Errors in u : (a) and du/dx ; (b) using 5-node irregular discretization.

study. The stabilized conforming (SC) nodal integration method displays a superior performance over the direct nodal integration and the five-point Gauss integration methods.

Next, quadratic basis functions are used in the mesh-free shape functions with a normalized support size of 2.4. The solution of u and du/dx using an equally spaced 9-node discretization are compared in Figures 13(a) and 13(b). The open circles in the figures represent the nodal locations. Severe oscillation in u is observed in the direct nodal integration method, and oscillation in du/dx near the boundary is also apparent. The proposed SC nodal integration completely eliminates oscillation in u and du/dx . The five-point Gauss integration method also generates a very good solution due to the use of regular discretization.

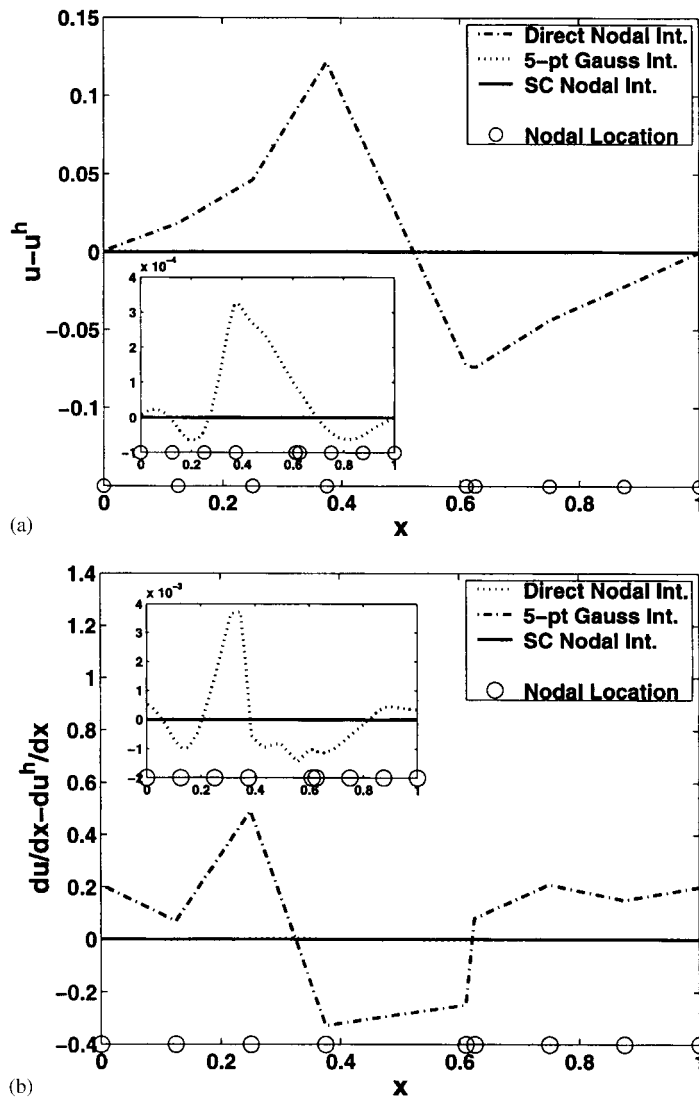


Figure 10. Errors in u : (a) and du/dx ; (b) using 9-node irregular discretization.

6.3. Problem with higher-order solution

Here we consider the following model problem:

$$-u_{,xx} + 20u = 0 \tag{58}$$

$$u_{,x}(0) = u_{,x}(1) = 1 \tag{59}$$

The shape functions are constructed using linear basis functions with normalized support size of 1.5. The comparison of u and du/dx using an equally spaced 11-node model is shown in Figures 14(a)

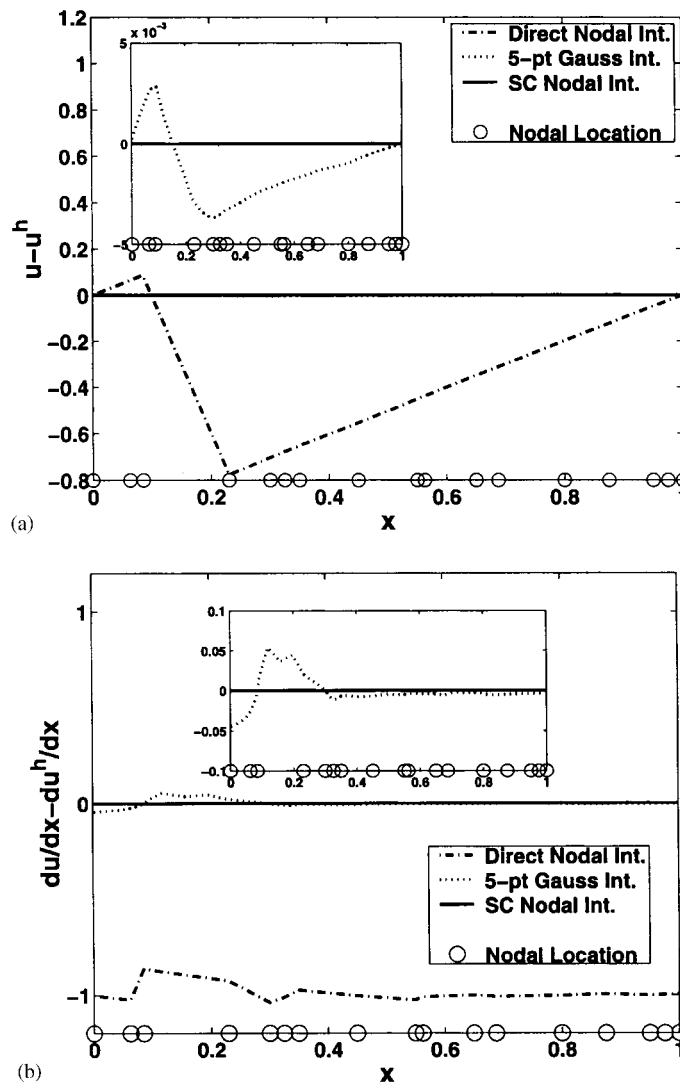


Figure 11. Errors in u : (a) and du/dx ; (b) using 17-node irregular discretization.

and 14(b). Although only small oscillation is observed in u using direct nodal integration, noticeable oscillation is presented in du/dx . Gauss integration and stabilized conforming (SC) nodal integration methods generate very good solution in u , but both produce some oscillation in du/dx , especially near the boundaries in Gauss integration.

Mesh-free models with 11, 21, 41, 81 equally spaced nodes are used in the convergence study. Normalized support size of 1.5 is used in all models. The L_2 norms of errors in u and du/dx are compared in Figures 15(a) and 15(b), respectively. Use of direct nodal integration in the Galerkin mesh-free method is clearly less accurate and displays lower rates of convergence and larger errors.

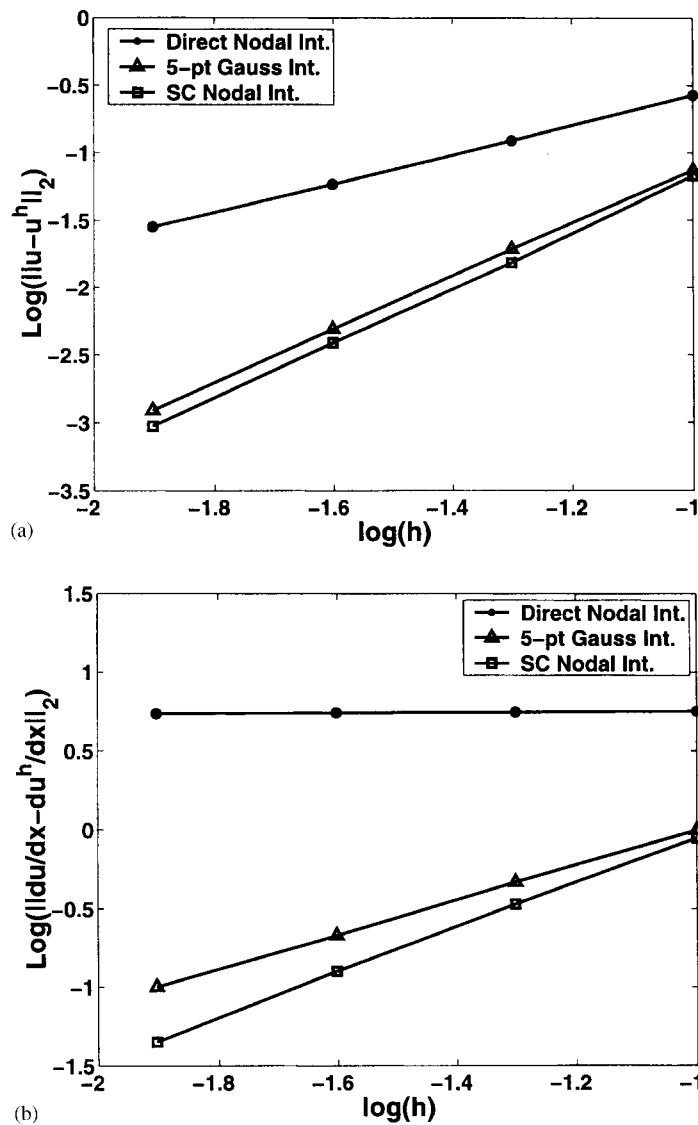


Figure 12. L_2 norms of errors in u : (a) and du/dx ; (b) in a bar problem using linear basis.

The enhanced accuracy in the SC nodal integration demonstrates the effectiveness of the proposed strain smoothing stabilization.

An irregular discretization is also studied. Shape function support size of 0.3 is used for all nodes; the maximum nodal distance is 0.16 in this discretization. Direct nodal integration displays severe oscillations in u and du/dx as shown in Figures 16(a) and 16(b). Circles in figures denote nodal locations. The larger error in the solution is related to the nodal space irregularity in the discretization. Oscillation in du/dx is also observed using Gauss integration. The SC nodal integration

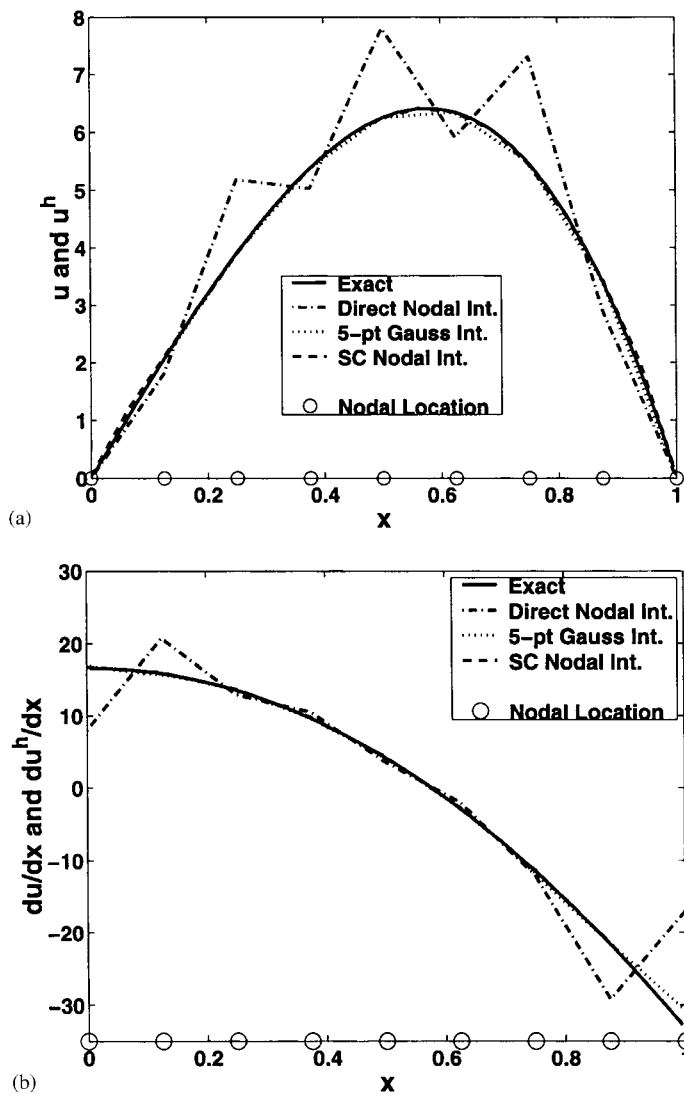


Figure 13. Comparison of u : (a) and du/dx ; (b) in a bar problem using quadratic basis.

method significantly improves solutions over the direct nodal integration method. Compared with solution by Gauss integration, the oscillation in du/dx near irregular nodes is reduced using SC nodal integration. However, noticeable error near the boundaries suggests that a model refinement is needed in those areas.

6.4. Example 4: Beam subjected to a shear load

In this problem, the accuracy and convergence in regular and irregular discretization of a beam problem using three integration methods are studied. The problem statement and boundary

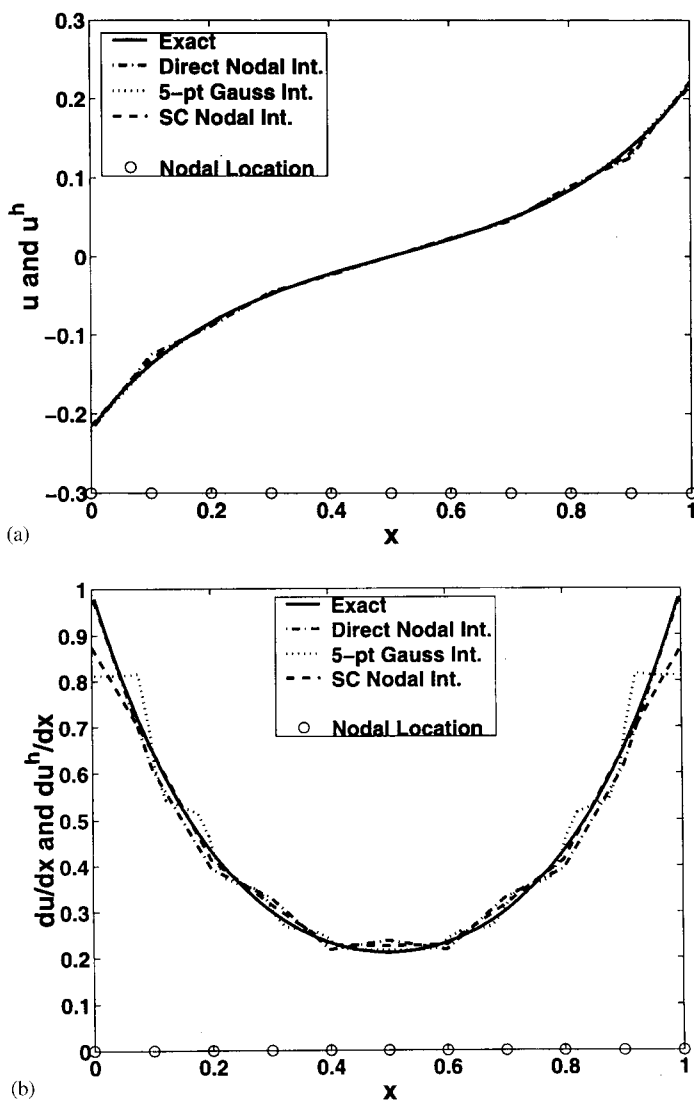


Figure 14. Comparison of u : (a) and du/dx ; (b) using a regular discretization.

conditions of the beam problem are given in Figure 17. Three regularly refined mesh-free discretizations for a half-model (anti-symmetry) are shown in Figure 18. Linear basis functions and a normalized support size of 2.01 are used in all three regular discretizations. A 5×5 quadrature is used for the Gauss integration method.

Superior performance of the stabilized conforming (SC) nodal integration over the direct nodal integration and Gauss integration methods is presented in the accuracy comparison of tip displacements in Table I. The direct nodal integration method displays a poor performance in the coarse model. SC nodal integration is particularly advantageous when a coarse model is used. A more

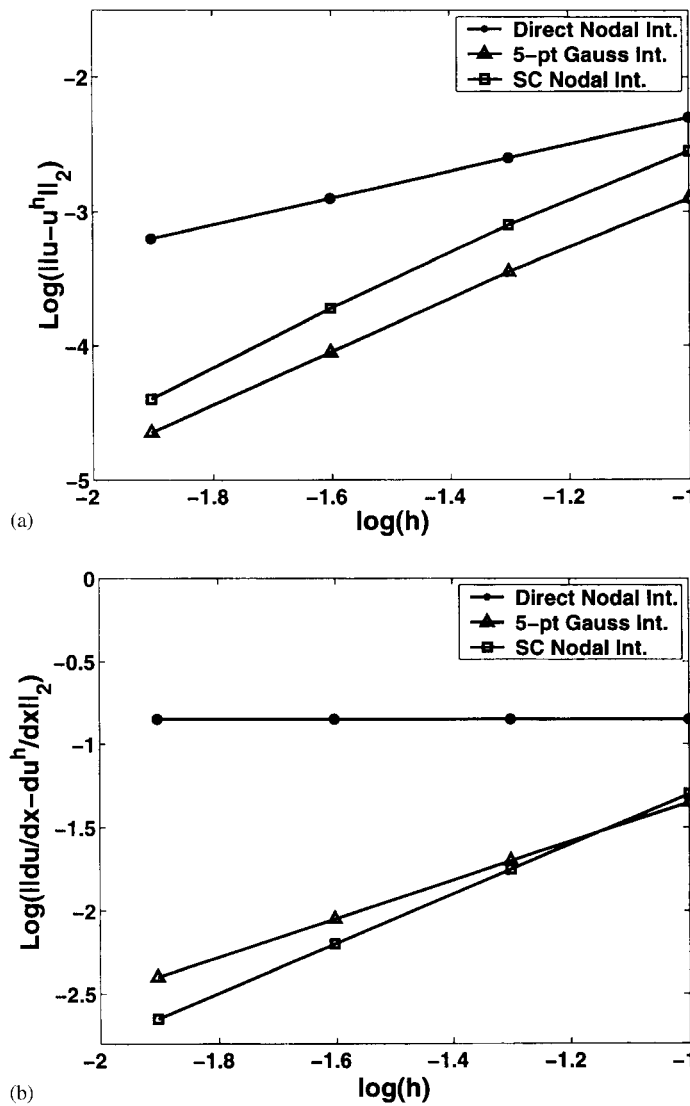


Figure 15. L_2 norms of errors in u : (a) and du/dx ; (b) using three integration methods.

detailed comparison of displacement solution along $y=0$ is shown in Figure 19. The displacement error norms are plotted in Figure 20. The solution of the direct nodal integration presents lower accuracy than that obtained from Gauss integration. SC nodal integration not only enhances accuracy of the direct nodal integration; the method performs better than the Gauss integration method. Shear stress along the $x=L/2$ of the 205-node model obtained from the direct nodal integration is shown in Figure 21(a), and for Gauss integration and SC nodal integration are plotted in Figure 21(b). Larger error near the boundary is observed in the solution of the direct nodal

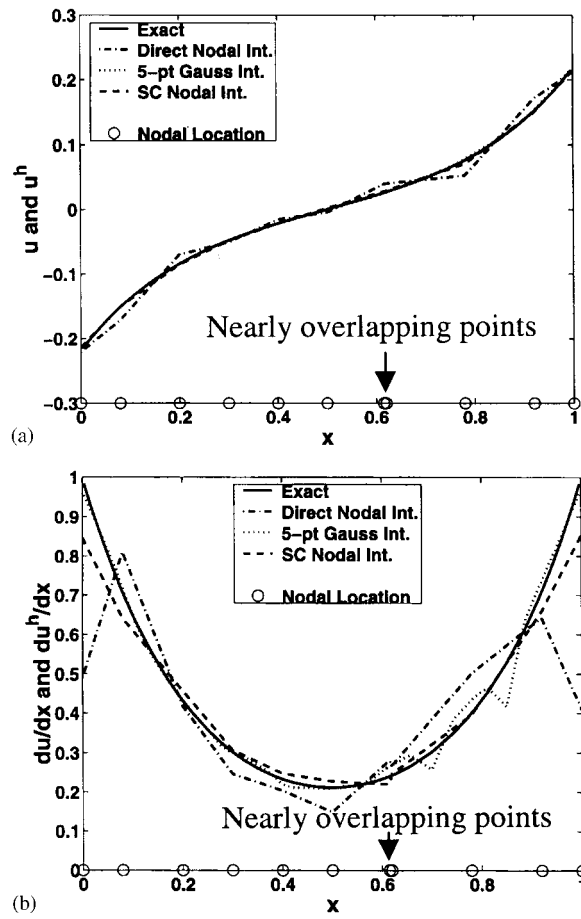


Figure 16. Comparison of u : (a) and du/dx ; (b) using an irregular discretization.

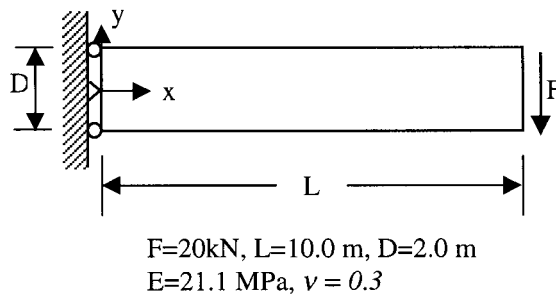


Figure 17. Problem statement of beam subjected to a shear load.

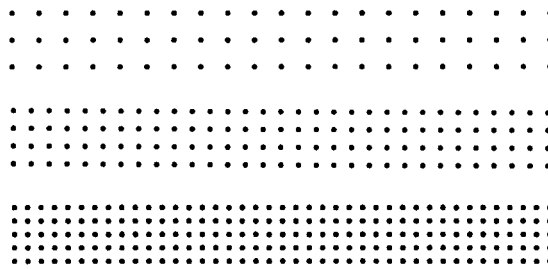


Figure 18. Regular discretization and refinement of half beam.

Table I. Tip displacement accuracy (%) using regular discretization.

Discrete model	5 × 5 Gauss int.	Direct nodal int.	SC nodal int.
63 nodes	93.4256	83.6453	97.3410
124 nodes	96.9630	91.9689	99.0507
205 nodes	98.2768	95.3838	99.5141

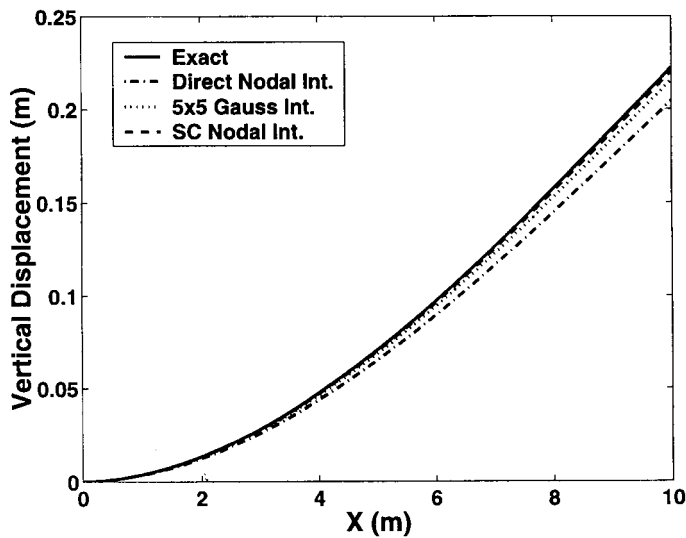


Figure 19. Comparison of vertical displacement along $y=0$ in beam problem.

integration, whereas Gauss integration and SC nodal integration methods generate similar results.

In Figure 22, several refinements of an irregular model are constructed to study the performance of three integration methods in irregular discretization. A Voronoi diagram for nodal integration methods is also plotted in Figure 22. The shape function support size in this study is increased slightly so that a normalized support size with respect to the maximum nodal distance is 2.01 in

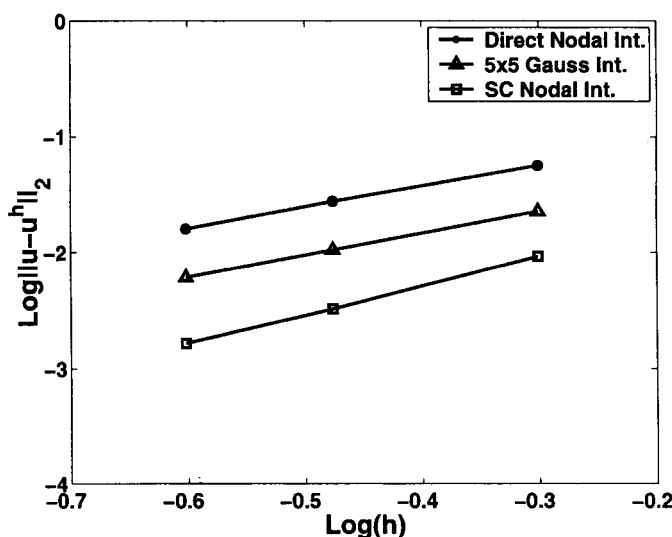


Figure 20. L_2 norms of displacement errors in regular discretization of a beam problem.

each model. Note that since support size is kept constant for all shape functions, the normalized support sizes in dense areas are higher than 2.01. Due to the slight irregularity in the discretization, the tip displacement accuracy of direct nodal integration and Gauss integration methods reduces slightly as shown in Table II. Surprisingly, the accuracy of SC nodal integration increases slightly compared to that of the regular case. This is probably due to the small increase in normalized support size in the dense areas compared to the regular model. The displacement distribution shown in Figure 23 further confirms the effectiveness of SC nodal integration. Figure 24 demonstrates that SC nodal integration converges better than the other two methods. The shear stress plot shown in Figure 25(a) displays a significant error in the direct nodal integration method. SC nodal integration not only improves accuracy in the direct nodal integration, it also predicts better solution than the Gauss integration method as demonstrated in Figure 25(b).

A very irregular 124-node model as shown in Figure 26 is created to test the performance of three methods under highly irregular discretization. Constant support size of 0.334 is used for all shape functions. Some regular nodes are placed in a small area for the purpose of comparing stress distributions across regular and irregular nodes. A Voronoi diagram for nodal integration is also plotted in Figure 26. The tip displacement solution of the direct nodal integration method deteriorates significantly in this case as shown in Table III. Surprisingly SC nodal integration still maintains a 99.25 per cent accuracy in the tip displacement; much better than direct nodal and Gauss integration methods. The comparison of displacement distribution along $y=0$ is also presented in Figure 27. Shear stress distribution along regular nodes at $x=0.5L$ in Figures 28(a) and 28(b) clearly demonstrate the superior performance of SC nodal integration over the other two methods. The shear stress distribution along irregular nodes at $x=0.6L$ in Figures 29(a) and 29(b) further shows the robustness of SC nodal integration in dealing with irregular discretization. A comparison of normalized CPU (with exclusion of equation solver) is given in Figure 30.

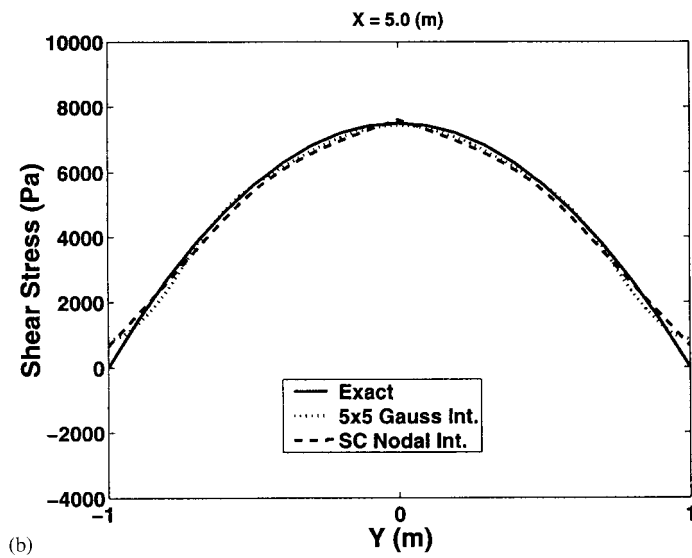
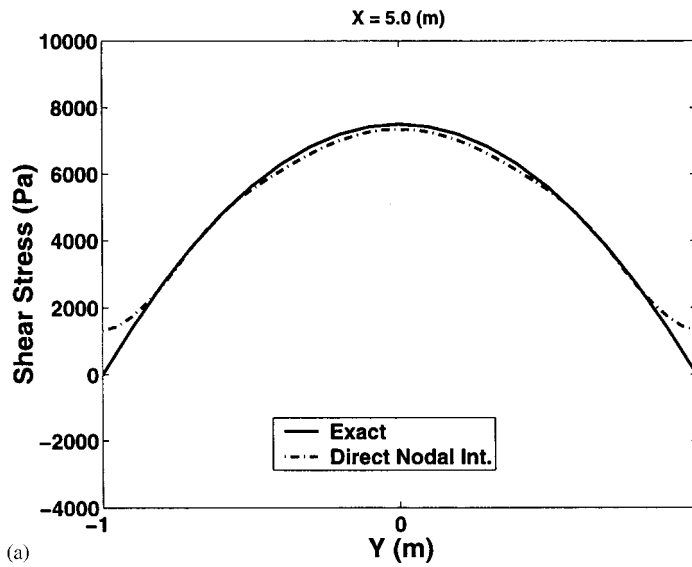


Figure 21. Comparison of shear stress distribution along $x = 0.5L$ in regular discretization.

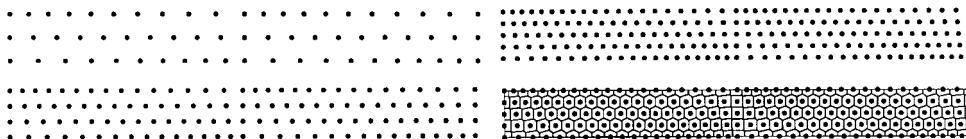
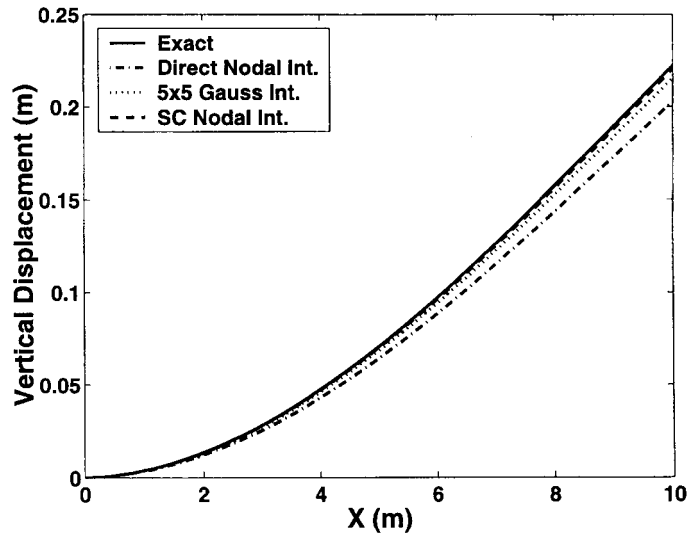
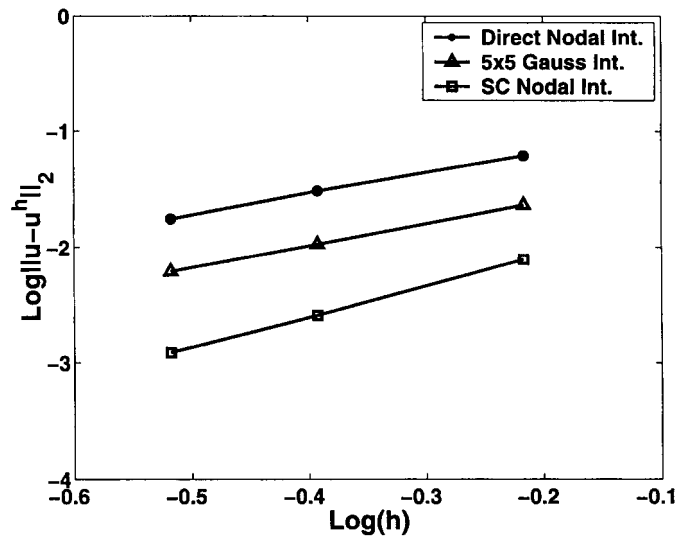


Figure 22. Irregular discretization, refinement, and Voronoi diagram of half-beam.

Table II. Tip displacement accuracy (%) using irregular discretization.

Discrete model	5 × 5 Gauss int.	Direct nodal int.	SC nodal int.
63 nodes	93.3411	82.3900	97.6919
124 nodes	96.9315	91.3030	99.2261
205 nodes	98.2183	95.0013	99.6221

Figure 23. Comparison of vertical displacement at $y=0$ in beam problem.Figure 24. L_2 norms of displacement errors in irregular discretization of a beam problem.

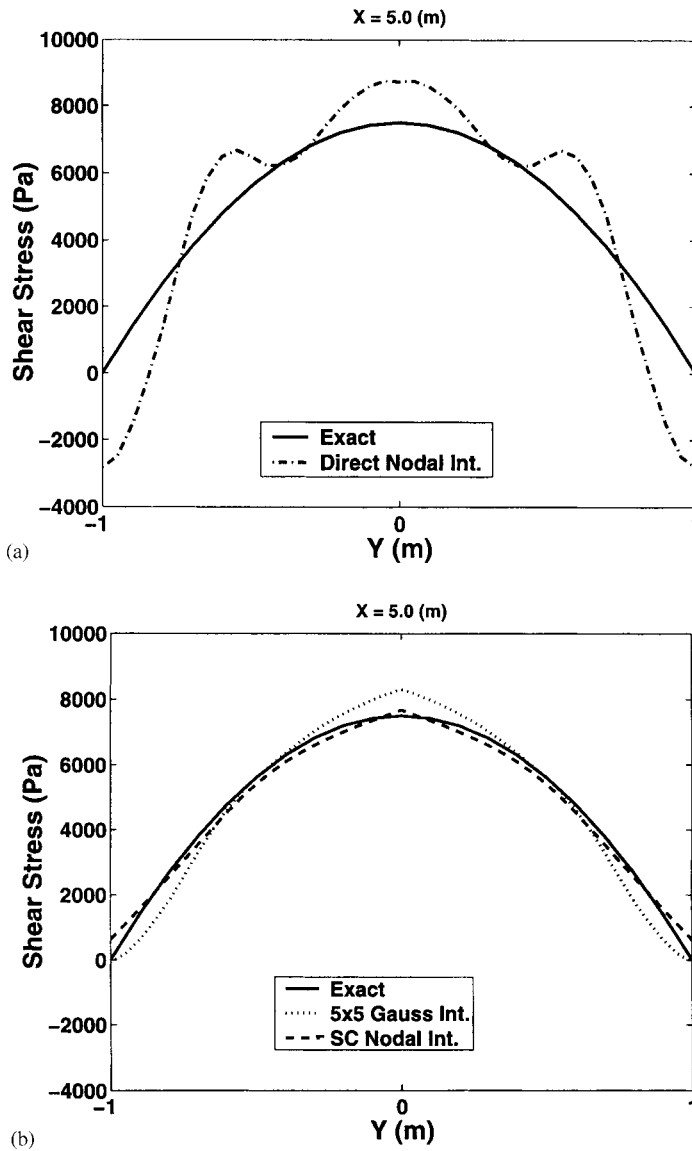


Figure 25. Comparison of shear stress distribution along $x = 0.5L$ in irregular discretization.

7. CONCLUSIONS

Mesh-free methods allow an unstructured discretization of a continuum. This property provides flexibility in the modelling of irregular geometry or localized phenomenon, but adds substantial complexity to the domain integration of the weak form. The completeness properties in the moving least-squares (MLS) and reproducing kernel (RK) approximation are not fully effective in the Galerkin approximation if the weak form is not properly integrated. In addition to the mismatch

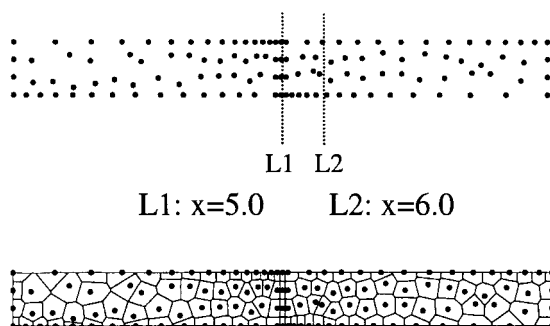


Figure 26. Beam with highly irregular discretization (124 nodes) and Voronoi diagram.

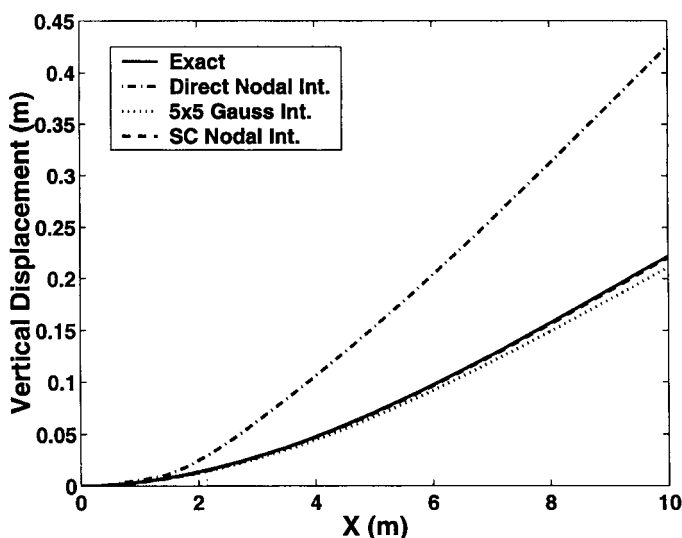


Figure 27. Comparison of displacement distribution along $y=0$ in a highly irregular model.

Table III. Tip displacement accuracy (%) using highly irregular discretization.

Discrete model	5 × 5 Gauss int.	Direct nodal int.	SC nodal int.
124 nodes	94.99	192.82	99.25

in the integration cells and the supports of shape functions [11], higher-order quadrature rules required in Gauss integration for Galerkin mesh-free methods is a major cause of high CPU. The use of a direct nodal integration is an attractive alternative from an efficiency standpoint, but the method suffers from its numerical instability and poor accuracy as shown in this paper.

It is also observed that mesh-free methods with linearly consistent shape functions generate significant errors in linear problems when direct nodal integration is used in an irregular discretization.

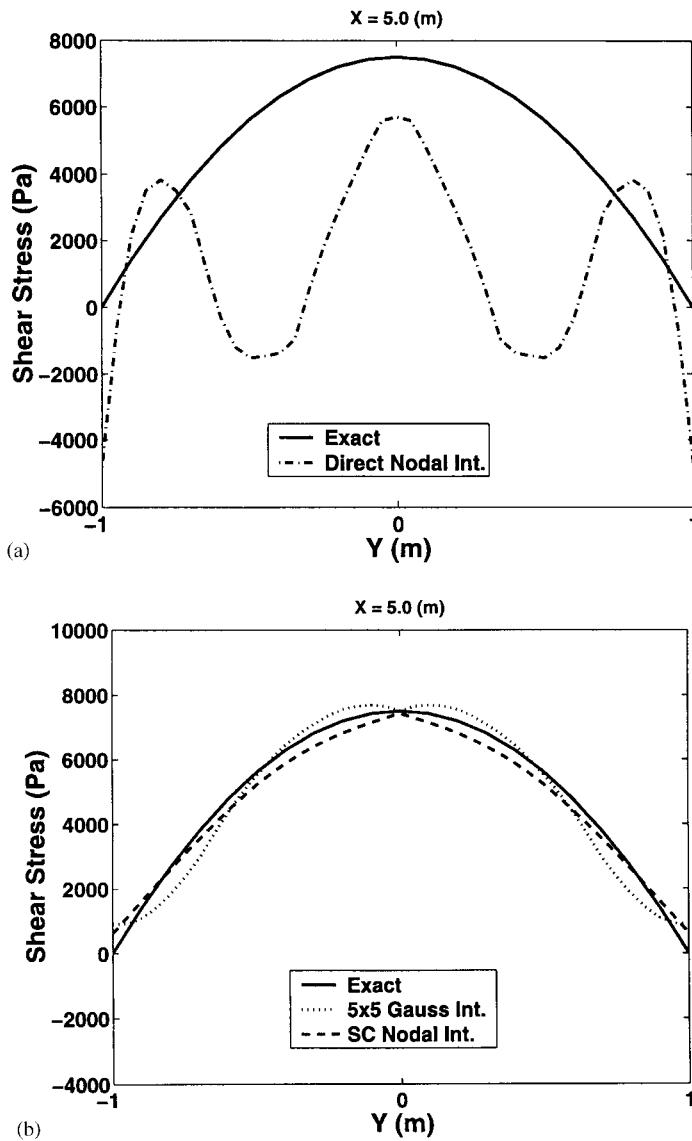


Figure 28. Comparison of shear stress distribution along $x = 0.5L$ in a highly irregular model.

Integration constraints (IC) are introduced based on the requirement for a linear displacement vector to satisfy the discrete equilibrium equation exactly. It is shown that a direct nodal integration significantly violates IC and thereby generates large error in linear problems. It is also demonstrated that Gauss integration does not fully satisfy IC at irregular discretization, and thus displays errors in linear problems.

To avoid instability due to the vanishing derivatives of shape functions at the nodes and to satisfy IC in the direct nodal integration, a strain smoothing stabilization is proposed. The strains

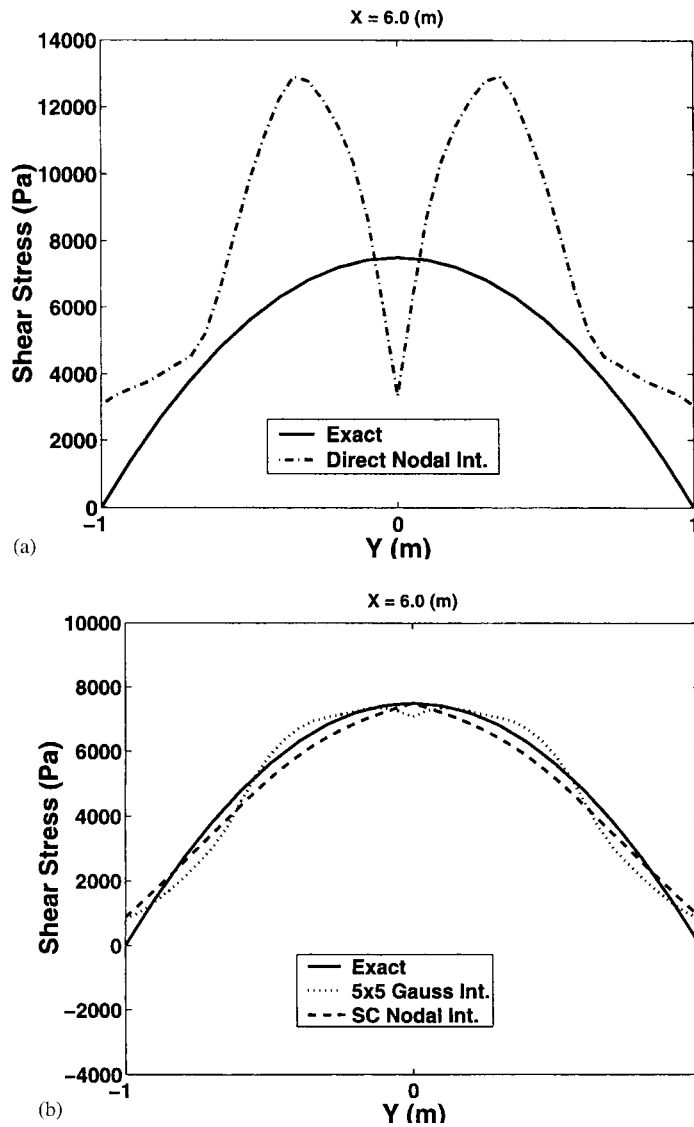


Figure 29. Comparison of shear stress distribution along $x = 0.6L$ in a highly irregular model.

are smoothed at the nodal points via a spatial averaging. By customizing the distribution function in the strain smoothing equation and using a divergence theorem to compute smoothed strain, the resulting smoothed gradient matrix satisfies IC. The construction of the smoothed gradient matrix requires an integration over the boundary of the nodal representative domain. A simple two- or three-point trapezoidal rule can be used for integration of each boundary segment without violating IC, and the computational procedure is rather efficient. An assumed strain method is used to formulate the Galerkin approximation using the smoothed strain and displacement as independent

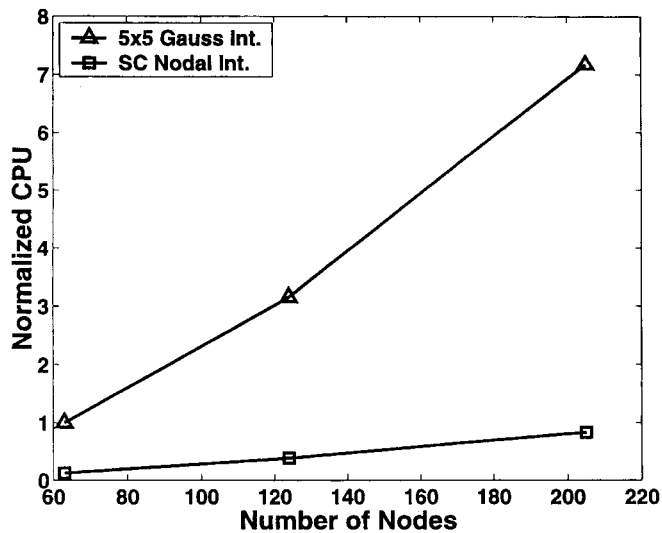


Figure 30. Comparison of normalized CPU (with exclusion of solving algebraic equation).

variables. The final discrete equilibrium equation is expressed in terms of displacement vectors, and the stiffness matrix is integrated entirely at nodal points. Since the smoothed gradient matrices are consistent with the weights in the nodal integration, the distribution of weights have marginal effect on the solution accuracy. Although a Voronoi diagram is used for obtaining representative nodal domain and the associated weights for the stabilized conforming nodal integration in this work, other simpler methods can also be used for this purpose.

The proposed method offers the following unique features:

1. The proposed strain smoothing method stabilizes spurious modes. The method also satisfies linear exactness in Galerkin approximation of an equilibrium equation. This property significantly enhances the numerical performance of the direct integration method. Further, since Gauss integration does not meet integration constraints, the proposed method provides better accuracy than the 5×5 Gauss integration method in several demonstration problems.
2. The need for a quadrature structure is eliminated in the proposed method. Evaluating stiffness matrix at the nodal points is substantially more efficient than using Gauss integration. Although the strain smoothing involves evaluation of shape functions at the vertices of the representative nodal domain, it is only needed for shape functions. The stiffness is integrated entirely at the nodes.
3. The proposed method is quite robust in dealing with irregular nodal spacing in mesh-free discretization. The numerical examples demonstrate that the superiority of the proposed method becomes more obvious in mesh-free discretization with higher irregularities.
4. No numerical control parameter is involved in the proposed strain smoothing stabilization. The performance of the proposed method appears to be quite independent to problem characteristics and domain discretization.

The extension of this method to non-linear problems requires smoothing on the deformation gradient that will be discussed in a separate paper. Three-dimensional problems will also be studied in the near future.

ACKNOWLEDGEMENTS

The Support of this work by NSF under the grant CMS 97-13842 and by the NSF/DARPA OPAAL Program under the grant DMS 98-74015 to the University of Iowa is greatly acknowledged.

REFERENCES

1. Nayroles B, Touzot G, Villon P. Generalizing the finite element method: diffuse approximation and diffuse elements. *Computational Mechanics* 1992; **10**:307–318.
2. Belytschko T, Lu YY, Gu L. Element-free Galerkin methods. *International Journal for Numerical Methods in Engineering* 1994; **37**:229–256.
3. Liu WK, Jun S, Zhang YF. Reproducing kernel particle methods. *International Journal for Numerical Methods in Fluids* 1995; **20**:1081–1106.
4. Chen JS, Pan C, Wu CT, Liu WK. Reproducing kernel particle methods for large deformation analysis of nonlinear structures. *Computer Methods in Applied Mechanics and Engineering* 1996; **139**:195–227.
5. Duarte CAM, Oden JT. A h-p adaptive method using clouds. *Computer Methods in Applied Mechanics and Engineering* 1996; **139**:237–262.
6. Melenk JM, Babuska I. The partition of unity finite element method: basic theory and applications. *Computer Methods in Applied Mechanics and Engineering* 1996; **139**:289–314.
7. Sulsky D, Chen Z, Schreyer HL. A particle method for history-independent materials. *Computer Methods in Applied Mechanics and Engineering* 1994; **118**:179–196.
8. Atluri SN, Zhu T. A new meshless local Petrov–Galerkin (MLPG) approach. *Computational Mechanics* 1998; **22**:117–127.
9. Monaghan JJ. An introduction to SPH. *Computer Physics Communications* 1988; **48**:89–96.
10. Randles PW, Libersky LD. Smoothed particle hydrodynamics: some recent improvements and applications. *Computer Methods in Applied Mechanics and Engineering* 1996; **139**:375–408.
11. Beissel S, Belytschko T. Nodal integration of the element-free Galerkin method. *Computer Methods in Applied Mechanics and Engineering* 1996; **139**:49–74.
12. Dolbow J, Belytschko T. Numerical integration of Galerkin weak form in meshfree methods. *Computational Mechanics* 1999; **23**:219–230.
13. Randles PW, Libersky LD, Petschek AG. On neighbors, derivatives, and viscosity in particle codes. *Proceeding of ECCM Conference*, Munich, Germany, 31 August–3 September 1999.
14. Bonet J, Kulasegaram S. Correction and stabilization of smooth particle hydrodynamics methods with applications in metal forming simulation. *International Journal for Numerical Methods in Engineering* 1999; **47**:1189–1214.
15. Belytschko T, Krongauz Y, Fleming M, Organ D, Liu WK. Smoothing and accelerated computations in the element-free Galerkin method. *Journal of Computational Applied Mathematics* 1996; **74**:111–126.
16. Breitkopf P, Touzot G, Villon P. Double grid diffuse collocation method. *Computational Mechanics* 2000; **25**:199–206.
17. Liszka T, Orkisz J. The finite difference method at arbitrary irregular grids and its application in applied mechanics. *Computer and Structures* 1980; **11**:83–95.
18. Krongauz Y, Belytschko T. Enforcement of essential boundary conditions in meshless approximations using finite elements. *Computer Methods in Applied Mechanics and Engineering* 1996; **131**:133–145.
19. Chen JS, Wang HP. New boundary condition treatments for meshless computation of contact problems. *Computer Methods in Applied Mechanics and Engineering* 2000; **187**:441–468.
20. Krongauz Y, Belytschko T. Consistent pseudo-derivatives in meshless methods. *International Journal for Numerical Methods in Engineering* 1997; **146**:371–386.
21. Johnson GR, Beissel SR. Normalized smoothing functions for impact computations. *International Journal for Numerical Methods in Engineering* 1996; **39**:2725–2741.
22. Chen JS, Wu CT. Generalized nonlocal meshfree method in strain localization. *Proceeding of International Conference on Computational Engineering Science*, Atlanta, Georgia, 6–9 October 1998.
23. Chen JS, Wu CT, Belytschko T. Regularization of material instabilities by meshfree approximations with intrinsic length scales. *International Journal for Numerical Methods in Engineering* 2000; **47**:1303–1322.
24. Simo JC, Hughes TJR. On the variational foundation of assumed strain methods. *ASME Journal of Applied Mechanics* 1986; **53**:51–54.